Weakly bound halo breakup of neutron-^{7}Li and nucleon-^{7}Be on a lead target

B. Mukeru [1,*] T. Frederico [2,†] and Lauro Tomio [3,‡]

[1]*Department of Physics, University of South Africa, P.O. Box 392, Pretoria 0003, South Africa*
[2]*Instituto Tecnológico de Aeronáutica, 12228-900, São José dos Campos, Brazil*
[3]*Instituto de Física Teórica, Universidade Estadual Paulista, 01140-070, São Paulo, Brazil*

(Received 13 October 2020; accepted 9 December 2020; published 28 December 2020)

A comparative analysis of the breakup cross-sections, using continuum discretized coupled-channel approach, is presented for the weakly bound p-wave neutron-^{7}Li and nucleon-^{7}Be projectiles on the ^{208}Pb target, by investigating the role of interaction effects between the core (^{7}Li, ^{7}Be) with the target. The extra charge in the ^{8}B has the effect to increase the Coulomb contribution in the breakup reaction channel. By fixing both projectile ground-state binding energies at 0.137 MeV (^{8}B experimental one), with incident energies at the Coulomb barrier and above, we found that the charge difference accounts for over 30% of the neutron-^{7}Be breakup cross sections, substantially larger than the corresponding one for proton-^{7}Be. The large enhancement of the neutron-halo breakup cross-section with respect to the proton-halo case shown in this work is associated to dynamical effects coming from the excitation of the projectile internal continuum due to the nucleon-target and core-target interactions, together with the widely accepted static effects coming from the long wave-function tail of the weakly bound neutron. The interplay between these dynamical and static effects in the energy spectrum of the ^{8}B fragments is visible, revealed by the peak of the energy distribution pushed to higher relative energies. This follows from the two-body final state interactions between the charged fragments distorted by the three-body reaction environment.

DOI: 10.1103/PhysRevC.102.064623

I. INTRODUCTION

Nucleon-halo breakups have been extensively investigated over the past few decades, as one can follow through some text books and available reviews [1–9], from where most relevant references can be accessed. Among them, several works can be pointed out closely related to proton- and neutron (n)-halo breakups, as Refs. [10–34]. However, besides the progress on this matter, a clear understanding of their similarities and/or differences remains one of the outstanding issues. The challenge of such comparative study arises from the fact that it involves many detailed properties, such as different ground-state configurations, binding energies, core masses and charges, among others. To focus on the relevant degrees of freedom, a proton (p) may be replaced by a neutron (n), keeping the same ground-state binding energy to obtain a "neutron-halo." In this case, one does not have to worry about different core masses and charges, as well as different ground-state configurations and energies, thus freezing an important number of these properties. Such procedure was adopted in Refs. [20,29,34], where the proton in the $^8\mathrm{B} \to {}^7\mathrm{Be}+\mathrm{p}$ system was replaced by a neutron (^{7}Be +n), building a fictitious "^{8}Be" nucleus, keeping the same ground-state configuration and binding energy. Also, in Ref. [21], a proton in the ^{16}O+p system was replaced by a neutron (^{16}O+n), for the same purpose of understanding the proton-and neutron-halo breakups. These studies, among many others, have established that the ground-state binding energy, namely the neutron or proton separation energy, as well as the proton charge are the main factors dictating the quantitative difference in the two breakup processes. When both the proton- and neutron-halo nuclei are considered as having, respectively, equal one-proton and one-neutron separation energies, the neutron-halo breakup cross sections are substantially larger than the proton-halo ones. This was understood as due to the peripheral extension of the neutron-halo ground-state function, with static effects becoming more relevant than the proton-halo case due to such peripherality of breakup processes.

The first motivation, to replace a proton by a neutron in such comparative studies, is to explore the role of the Coulomb interaction in the three-body dynamics, characterized by the coupling between the initial state with the nucleon-core continuum. Particularly in Coulomb-dominated reactions, as in the case of a lead target, the extra charge in the core/halo are expected to be relevant in the reaction process. However, not only such dynamical effects are yet to be comprehensively established, but also it is not clear whether the same core nucleus produces similar effects in the proton-and neutron-halo breakup. To the best of our knowledge, there is no comparative study along this line.

The second motivation is that the separation between Coulomb and nuclear cross sections was proved to be unambiguously difficult to be undertaken within a single reaction [27], reinforcing the necessity to perform comparative studies with other projectiles with the same mass but with different

*mukerb1@unisa.ac.za
†tobias@ita.br
‡lauro.tomio@unesp.br

charges (in the core or in the halo). Moreover, the interplay of the static and dynamical effects, coming from the three-body reaction mechanism, remains to be clarified. Such investigation, albeit qualitative, would pave the way towards a better understanding of the similarities and/or differences in the proton- and neutron-halo breakup, and in addition the role of the core and its charge in the process.

In this work, we study the breakups of ^{8}B and ^{8}Li nuclei on a lead target, in an effort to contribute towards a better understanding of the proton- and neutron-halo breakup dynamics. These are two mirror nuclei, having similar ground-state configurations and atomic masses. When modeled as two-body proton and neutron halos ($^8\mathrm{B} \to {}^7\mathrm{Be}+\mathrm{p}$, $^8\mathrm{Li} \to {}^7\mathrm{Li}+\mathrm{n}$), the two ^{7}Be and ^{7}Li core nuclei are as well mirror nuclei, and their charges differ by one unit. To better study the static and dynamical effects, we analyze three different reactions, namely, $^7\mathrm{Be}+\mathrm{p}+{}^{208}\mathrm{Pb}$, $^7\mathrm{Li}+\mathrm{n}+{}^{208}\mathrm{Pb}$, and the fictitious $^7\mathrm{Be}+\mathrm{n}+{}^{208}\mathrm{Pb}$. The third reaction is included in our analysis by considering that both ^{7}Be +n and ^{7}Li +n would have the same ground-state and continuum wave functions, leading to similar static effect on the breakup cross sections. Then, the difference in their dynamics will be due to the charge of the extra proton in the ^{7}Be with respect to ^{7}Li. Therefore, the ^{7}Be +n and ^{7}Li +n breakup cross sections on the same target will provide a better picture on how the dynamical effect due to the ^{7}Li-target interaction changes when the proton in the ^{7}Be +p system is replaced by a neutron. In particular, with the same ground-state binding energy, we intend to investigate whether the longer tail of the corresponding wave function alone could justify the substantial enhancement of the neutron-halo breakup cross section, compared to the proton-halo breakup.

However, these reactions with heavy target are Coulomb-dominated, having the Coulomb breakup controlled by dipole transitions, which according to the first-order approximation theory [35–38], is directly proportional to the electric dipole response function, dependent on the effective charge. For the first-order multipole transition, the ^{7}Be +n system has the large effective charge, while decreases for ^{7}Be +p and ^{7}Li +n systems. This implies that considering the same ground-state binding energy, the electric dipole response function of the ^{7}Be +n will be larger than that of the ^{7}Li +n, even though they are expected to have similar bound and continuum wave functions, and hence the total and Coulomb breakup cross sections of the former system will be enhanced with respect to those of the latter system, due to the charge of the extra proton in the ^{7}Be. Our aim is to determine how important these cross sections are. As the three reactions have different Coulomb barriers height, V_B (49.36 MeV, 38.91 MeV and 28.65 MeV, respectively, for $^8\mathrm{B}+{}^{208}\mathrm{Pb}$, "^{8}Be" $+{}^{208}\mathrm{Pb}$, and $^8\mathrm{Li}+{}^{208}\mathrm{Pb}$ reactions, obtained with the São Paulo potential (SPP) [39]), with important breakup features occurring around the barrier, we consider the center-of-mass (c.m.) incident energy $E_\mathrm{c.m.}$ at the barrier and slightly above, with $E_\mathrm{c.m.}/V_\mathrm{B} = 1.0$ and 1.5. To check the dependence of the results on the ground-state binding energy, for each reaction, two different calculations will be performed for separation energies of $\varepsilon_0 = 0.137$ MeV and for $\varepsilon_0 = 2.033$ MeV, which are the ground-state binding energies of ^{7}Be +p and ^{7}Li +n systems, respectively. Our theoretical approach to obtain the different breakup cross sections is the continuum discretized coupled-channels (CDCC) method [40].

In the next Sec. II, we present the model approach, in which some details on our numerical procedure are in Sec. II C. The main results are presented in Sec. III, together with the corresponding analysis. Finally, our conclusions are in Sec. IV.

II. MODEL FRAMEWORK

The interaction of a nucleon-core projectile with a target, in which μ_cn and μ_pt are the projectile core-nucleon and projectile-target reduced masses, respectively, is given by the three-body Hamiltonian

$$H_\mathrm{3B} = -\frac{\hbar^2}{2\mu_\mathrm{pt}}\nabla^2_{\mathbf{R}} + U_\mathrm{pt}(\mathbf{r},\mathbf{R}) + \left[-\frac{\hbar^2}{2\mu_\mathrm{cn}}\nabla^2_r + V_\mathrm{cn}(\mathbf{r})\right], \quad (1)$$

where the projectile core-nucleon Hamiltonian, with the corresponding core-nucleon interaction V_cn, is within square brackets. $U_\mathrm{pt}(\mathbf{r},\mathbf{R})$ is the optical model potential, with $\mathbf{R}$ and $\mathbf{r}$ being, respectively, the projectile-target (pt) and projectile-core-nucleon (cn), c.m. vectors. As our present study is concerned with a nucleon-core projectile with eight nucleon, we also define the core-target (ct) and nucleon-target (nt) vector positions, respectively, by $\mathbf{R}_\mathrm{ct} \equiv \mathbf{R} + \frac{1}{8}\mathbf{r}$ and $\mathbf{R}_\mathrm{nt} \equiv \mathbf{R} - \frac{7}{8}\mathbf{r}$, such that the projectile-target optical potential can be expressed by the respective nuclear and Coulomb contributions of the nucleon-target and core-target, given by

$$U_\mathrm{pt}(\mathbf{r},\mathbf{R}) = \left[V^\mathrm{nucl}_\mathrm{ct}(\mathbf{R}_\mathrm{ct}) + \mathrm{i}W_\mathrm{ct}(\mathbf{R}_\mathrm{ct})\right] + V^C_\mathrm{ct}(\mathbf{R}_\mathrm{nt}) + \left[V^\mathrm{nucl}_\mathrm{nt}(\mathbf{R}_\mathrm{nt}) + \mathrm{i}W_\mathrm{nt}(\mathbf{R}_\mathrm{nt})\right] + V^C_\mathrm{nt}(\mathbf{R}_\mathrm{nt}), \quad (2)$$

where $W_\mathrm{ct(nt)}$ refer to the ct(nt) imaginary terms, which accounts for the projectile flux absorption by the target. The real and imaginary nuclear terms, as well as the central nuclear part of the core-nucleon interaction, V_cn, are generally expressed by Woods-Saxon form-factors, as

$$V_\mathrm{WS}(\mathbf{r}) = \left\{V_0 + V_\mathrm{so}\frac{\mathbf{j}\cdot\mathbf{I}}{r}\frac{d}{dr}\right\}\left[1+\exp\left(\frac{r-R_0}{a_0}\right)\right]^{-1}, \quad (3)$$

where the spin-orbit ($\mathbf{j}\cdot\mathbf{I}$) contribution V_so is assumed nonzero only for the core-nucleon system. All the other parameter definitions, as the interaction range R_0 and diffuseness a_0 for the respective two-body interactions will be clarified within details of our results.

The Coulomb interactions between the charged terms (V^C_ct, V^C_nt and V^C_cn, in which the last two are zero when the valence nucleon is the neutron), with respective electric charges Z_1e and Z_2e, can be formally written in terms of the step function [$\Theta(x) = 1(x>0)$, $\frac{1}{2}(x=0)$, $0(x<0)$]:

$$V^C(r) = Z_1Z_2e^2\left[\left(3-\frac{r^2}{R_C^2}\right)\frac{\Theta(R_C-r)}{2R_C} + \frac{\Theta(r-R_C)}{r}\right], \quad (4)$$

where R_C (Coulomb radius) defines the internal region.

A. CDCC approach brief description

Within the CDCC approach [40], the eigenstates of the internal core-nucleon Hamiltonian [inside the total

Hamiltonian Eq. (1), in which we have the relative core-nucleon momentum given by k], are expressed as a sum of radial $u^{J_p}_{k\ell}(r)$, angular and spin functions, where we also have the core and proton/neutron internal wave functions (with the core assumed structureless for the sake of simplicity), with the corresponding set of quantum numbers $\alpha \equiv (\ell, s, j, I, J_p)$ describing the projectile state, where ℓ is associated with the coordinate $\mathbf{r}$, with s and I the nucleon and core [^{7}Be(^{7}Li)] spins, respectively, and $\mathbf{j} = \ell + \mathbf{s}$ and $\mathbf{J}_p = \mathbf{j} + \mathbf{I}$. In the asymptotic region, the radial wave functions $u^{J_p}_{k\ell}$ are normalized according to

$$u^{J_p}_{k\ell}(r) \overset{r\to\infty}{\to} F_\ell(\eta, kr)\cos\delta_{\ell j}(k) + G_\ell(\eta, kr)\sin\delta_{\ell j}(k), \quad (5)$$

where $\delta_{\ell j}(k)$ are the nuclear phase shifts and F_ℓ, G_ℓ the Coulomb functions [41], given in terms of the Sommerfeld parameter $\eta = \frac{\mu_{\rm cn}}{\hbar^2}\frac{Z_c Z_n e^2}{k}$ and Coulomb phases $\sigma^\ell_\eta(k)$.

To describe the breakup process of the projectile, one needs to consider the exact scattering wave functions in the final state of the projectile, expanded in terms of the eigenstates of the internal core-nucleon. With respect to the bound-state wave function, we need the corresponding replacement of the quantum numbers α by α_0, where $\alpha_0 \equiv (\ell_0, s, j_0, I, \tilde{J}_0)$, with $\tilde{J}_0 = j_0 + I$, $j_0 = \ell_0 + s$ being the quantum numbers identifying the projectile ground-state. The radial ground-state $u^{\tilde{J}_0}_{k_0\ell_0}(r)$ is represented asymptotically by Whitaker functions [41],

$$u^{\tilde{J}_0}_{k_0\ell_0}(r) \overset{r\to\infty}{\to} C_0 W_{-\eta,\ell_0+\frac{1}{2}}(2k_0 r), \quad (6)$$

where $k_0 = {\rm i}\sqrt{2\mu_{\rm cn}|\varepsilon_{\alpha_0}|/\hbar^2}$ ($\varepsilon_{\alpha_0} \equiv -\varepsilon_0$ is the ground-state energy) and C_0 is the asymptotic normalization.

Let $\Psi^{JM}_{\mathbf{K}_\beta}(\mathbf{r}, \mathbf{R})$ be the three-body $(c + n + t)$ eigenfunction of Eq. (1), where $\beta \equiv (\alpha_0, \alpha)$, with the c.m. final linear momentum $\mathbf{K}_\alpha$ is related to the initial one $\mathbf{K}_{\alpha_0}$ by energy conservation, i.e., $\hbar^2 K^2_\alpha/(2\mu_{\rm pt}) + \varepsilon_\alpha = \hbar^2 K^2_{\alpha_0}/(2\mu_{\rm pt}) + \varepsilon_{\alpha_0}$, where the entrance channel energy is $E \equiv \hbar^2 K^2_{\alpha_0}/(2\mu_{\rm pt})$. The exact three-body wave function, $\Psi^{JM}_{\mathbf{K}_\beta}(\mathbf{r}, \mathbf{R})$, is then approximated as follows:

$$\Psi^{JM}_{\mathbf{K}_{\beta_i}}(\mathbf{r}, \mathbf{R}) = \sum_L \sum_{i=0}^{N_b} \frac{\chi^{LJ}_{\alpha_i}(R)}{R}\mathcal{G}^{LJ}_{\alpha_i}(\mathbf{r}, \Omega_{\mathbf{R}}), \quad (7)$$

where β_i is representing the set of quantum numbers given by (α_0, α_i), $\alpha_i \equiv (i, \ell, s, j, I, J_p)$, and N_b is the number of bins ($i = 0$ corresponds to the ground state). $\chi^{LJ}_{\beta_i}(R)$ are the expansion coefficients, given by the three-body radial wave functions describing the core-fragment c.m. motion relative to the target, with linear momenta $\boldsymbol{K}_{\beta_i}$, where L is the $\mathbf{R}$-associated orbital angular momentum quantum number (with $\Omega_{\mathbf{R}}$ the corresponding solid angle). The total angular momentum quantum number with the respective z projection are given by (J, M), where $\mathbf{J} = \mathbf{L} + \mathbf{J_p}$. The functions $\mathcal{G}^{LJ}_{\alpha_i}(\mathbf{r}, \Omega_{\mathbf{R}})$ provide the coupling of the direct product of the projectile wave function $\Phi_{\alpha_i}(\mathbf{r})$ with the corresponding target angular part, given by

$$\mathcal{G}^{LJ}_{\alpha_i}(\mathbf{r}, \Omega_{\boldsymbol{R}}) = [i^L \Phi_{\alpha_i}(\mathbf{r}) \otimes Y_L(\Omega_{\mathbf{R}})]_{JM}, \quad (8)$$

where, by using the CDCC binning approach [40,42], $\Phi_{\alpha_i}(\mathbf{r})$ contains the square integrable bin wave functions $\phi^{J_p}_{k_i\ell}(r)$ ($i = 1, 2, \ldots, N_b$), which are expressed by [6]

$$\phi^{J_p}_{k_i\ell}(r) = \sqrt{\frac{2}{\pi W_{\alpha_i}}}\int_{k_{i-1}}^{k_i} {\rm g}_{\alpha_i}(k)\, u^{J_p}_{k\ell}(r)dk, \quad (9)$$

where ${\rm g}_{\alpha_i}(k)$ is the weight function, with $W_{\alpha_i} = \int_{k_{i-1}}^{k_i} {\rm g}_{\alpha_i}(k)\, dk$ the normalization coefficient, such that $\langle\phi^{J_p}_{k_i\ell}|\phi^{J_p}_{k_i\ell}\rangle = 1$. The bin momenta k_i are obtained by truncating the linear momentum to $k_{\rm max}$, within the interval $[0, k_{\rm max}]$ discretized into bins of width $\Delta k_i = k_i - k_{i-1}$, with each bin energy being

$$\varepsilon_{\alpha_i} = \frac{\hbar^2}{2\mu_{\rm cn} W_{\alpha_i}}\int_{k_{i-1}}^{k_i} k^2 \left|{\rm g}_{\alpha_i}(k)\right|^2 dk. \quad (10)$$

So, after the projectile eigenstates are expanded in terms of the above $\phi^{J_p}_{k_i\ell}(r)$, and considering the Eq. (7), the corresponding Hamiltonian eigenvalue equation is represented by the following coupled differential equation for the coefficients $\chi^{LJ}_{\beta_i}(R)$:

$$\left[-\frac{\hbar^2}{2\mu_{\rm pt}}\left(\frac{d^2}{dR^2} - \frac{L(L+1)}{R^2}\right) + U^{LJ}_{\beta_i\beta_i}(R)\right]\chi^{LJ}_{\beta_i}(R) + \sum_{\beta_i\neq\beta'_i} U^{LL'J}_{\beta_i\beta'_i}(R)\chi^{L'J}_{\beta'_i}(R) = \left[E - \varepsilon_{\beta_i}\right]\chi^{LJ}_{\beta_i}(R), \quad (11)$$

where E is the incident energy. These equations are numerically solved, with the usual asymptotic conditions,

$$\chi^{LJ}_{\beta_i}(R) \overset{R\to\infty}{\to} \frac{i}{2}\left[H^-_L(K_{\beta_i}R)\delta_{\beta_i\beta'_i} - H^+_L(K_{\beta_i}R)S^J_{\beta_i\beta'_i}(K_{\beta_i})\right],$$

where $H^\pm_L(K_{\alpha_i}R)$ are the Coulomb-Hankel functions [41], and $S^J_{\beta_i\beta'_i}(K_{\beta_i})$ the breakup S-matrix. In Eq. (11), $U^{LJ}_{\beta_i\beta_i}(R) = U^{LJ}_{\alpha_0\alpha_0}(R) + U^{LJ}_{\alpha_i\alpha_i}(R)$ and $U^{LL'J}_{\beta_i\beta'_i}(R) = U^{LL'J}_{\alpha_0\alpha_i}(R) + U^{LL'J}_{\alpha_i\alpha'_i}(R)$ are diagonal and off-diagonal coupling matrix elements, which couple different states of the projectile after its interaction with the target nucleus. The potential $U_{\rm pt}(\mathbf{r}, \mathbf{R})$ given by Eq. (2), once integrated on $\mathbf{r}$ and angles, can be written as

$$U^{LL'J}_{\beta_i\beta'_i}(R) = \left\langle\mathcal{G}^L_{\beta_i}(\mathbf{r}, \Omega_R)\middle|U_{\rm pt}(\mathbf{r}, \mathbf{R})\middle|\mathcal{G}^{L'}_{\beta'_i}(\mathbf{r}, \Omega_R)\right\rangle. \quad (12)$$

Once Eq. (11) is solved, the differential and integrated expressions for the breakup cross section can be directly obtained from the corresponding breakup matrix, $S_{\alpha_i\alpha'_i} \equiv S_{\alpha_i\alpha'_i}(K_{\alpha_i})$ [27], such that

$$\sigma(E) \equiv \int d\Omega \frac{d\sigma(E)}{d\Omega} \equiv \sum_L \sigma_L(E) \equiv \frac{\pi}{K^2_{\alpha_0}}\sum_{J\alpha_i L\alpha'_i L'}\frac{2J+1}{2\tilde{J}_0+1}|S_{\alpha_i\alpha'_i}|^2. \quad (13)$$

In the above, we are also identifying the partial angular momentum contribution, $\sigma_L(E)$, obtained from the rearrangement of the summations [27]. From Eq. (13), we can also extract $d\sigma/d\varepsilon$, the differential cross-section for the relative core-nucleon energy distribution ε.

B. Projectile electric response functions

In the asymptotic region, where only Coulomb forces are available, $U_{\rm pt}(\mathbf{r},\mathbf{R}) \to V^C(\boldsymbol{r},\boldsymbol{R})$, can be expanded as

$$U_{\rm pt}(\mathbf{r},\mathbf{R}) \overset{R\to\infty}{\to} 4\pi Z_t e \sum_\lambda \frac{\sqrt{2\lambda+1}}{R^{\lambda+1}} \left[\mathcal{M}^\varepsilon_\lambda(\mathbf{r}) \otimes Y_\lambda(\Omega_{\boldsymbol{R}})\right]_{\lambda 0}, \tag{14}$$

where $Z_t e$ is the target charge, λ the multipole order, with $\mathcal{M}^\varepsilon_\lambda(\boldsymbol{r}) \equiv Z_\lambda r^\lambda Y^\mu_\lambda(\Omega_r)$ (Z_λ is the effective charge) being the projectile electric operator, given by

$$\mathcal{M}^\varepsilon_\lambda(\mathbf{r}) = e\left[Z_n\left(\frac{A_c}{A_p}\right)^\lambda + Z_c\left(-\frac{A_n}{A_p}\right)^\lambda\right] r^\lambda Y_\lambda(\Omega_{\boldsymbol{r}}). \tag{15}$$

This equation singles out the core charge relevance in the neutron-halo Coulomb breakup, where $Z_n = 0$. The Coulomb breakup in the asymptotic region is known to be directly related to the projectile internal structure. For the transition from the ground to continuum, the projectile electric response function is expressed by

$$\frac{dB(E\lambda)}{d\varepsilon} = \frac{\mu_{\rm cn}}{\hbar^2 k} \sum_{J_p} \hat{J}_p^2 |\langle((\ell s)jIJ_p|Y_\lambda(\Omega_{\boldsymbol{r}})|(\ell_0 s)j_0 I\tilde{J}_0\rangle \times \left|\int_0^\infty dr u^{J_p}_{k\ell}(r) r^\lambda u^{\tilde{J}_0}_{k_0\ell_0}(r)\right|^2, \tag{16}$$

where the pure continuum wave functions $u^{J_p}_{k\ell}(r)$ could be replaced by the continuum bin wave functions $\phi^{J_p}_{k_i\ell}(r)$. However, in our case, there is no need to do that since the radial integral $\int_0^\infty dr u^{J_p}_{k\ell}(r) r^\lambda u^{\tilde{J}_0}_{k_0\ell_0}(r)$ has no convergence issues. Nevertheless, this replacement could be useful for transitions between continuum states. Following Refs. [35–38,43], one can show that the Coulomb dipole breakup cross section is related to the projectile dipole electric function Eq. (16), given by

$$\frac{d\sigma^{E1}_C}{d\varepsilon} = \frac{32\pi^2}{9}\left(\frac{Z_t e}{\hbar v}\right)^2 z_m \mathcal{K}_0(z_m)\mathcal{K}_1(z_m)\frac{dB(E1)}{d\varepsilon}, \tag{17}$$

where $\mathcal{K}_{0(1)}(z)$ are the second kind modified Bessel functions of order 0(1) [41], with z_m, related to the minimum impact parameter $b_{\rm min}$, defined as

$$z_m \equiv \frac{\varepsilon-\varepsilon_0}{\hbar v} b_{\rm min} = \frac{\varepsilon-\varepsilon_0}{\hbar v}\left[\frac{Z_p Z_t e^2}{2E\tan(\theta_c/2)}\right], \tag{18}$$

where θ_c is the maximum cutoff scattering angle up to which the Coulomb breakup is dominant.

C. Numerical details and parameters

The physical inputs required for the numerical solution of the coupled differential Eqs. (11) are described in the following, together with the core-nucleon potential parameters, as well as the parameters of the projectile-target optical potentials. The experimental ground-state (p-wave) energies of the projectiles ^{8}B and ^{8}Li are, respectively, $\varepsilon_0 = 0.137$ MeV and 2.033 MeV [44], with quantum numbers $\ell = 1$ and $j^\pi = 2^+$. These states are obtained by coupling the proton (neutron) in the $0p_{\frac{3}{2}}$ orbit with the $\frac{3}{2}^-$ ground state of the core nucleus ^{7}Be (^{7}Li). In addition to the ground state, the ^{8}Li also exhibits an excited bound state ($j^\pi = 1^-$), with energy $\varepsilon_{\rm ex} = 0.98$ MeV [44]. The projectile bound and continuum wave functions are obtained from the solution of the corresponding Schrödinger equation, using core-nucleon Woods-Saxon potentials, whose parameters are summarized in Table I. All partial waves are contributing to the core-nucleon interactions through the angular momentum dependence of the potential spin-orbit coupling term, expressed by the Eq. (3), in which a common value $V_{\rm so} = -19.59\,\text{MeVfm}^2$ was assumed.

TABLE I. Core-nucleon potential depths with respective binding energies used for the ^{7}Be +p, ^{7}Be +n and ^{7}Li +n systems. For the spin-orbit part, we have considered a common value $V_{\rm so} = -19.59\,\text{MeV fm}^2$. The range and diffuseness parameters (nuclear and spin-orbit), are also assumed the same, respectively, $R_{\rm so} = R_0 = 2.391$ fm, with $a_{\rm so} = a_0 = 0.52$ fm. For ^{7}Be +p we also take $R_C = 2.391$ fm.

System	ε_0(MeV)	$-V_0$(MeV)
^{7}Be +p	0.137	44.65
	2.033	49.80
^{7}Be +n	0.137	38.23
	2.033	44.25
^{7}Li +n	0.137	38.23
	2.033	44.25

The parameters for the ^{7}Be +p system were taken from Ref. [45]. The same nuclear parameters were used for the ^{7}Li +n system, where the depth of the central part was adjusted to fit the ground state as well as excited bound-state energies. The same approach was adopted to the ^{7}Be+n system.

In Table II, we summarize the parameters of the core-target and nucleon-target optical potentials. The ^{7}Be-target optical potential parameters are from Ref. [46], with those for ^{7}Li-target are from the global parametrization of Ref. [47]. Those for the nucleon-target are from the global parametrization of Ref. [48]. In the considered incident energy range, the

TABLE II. Potential parameters for ^{7}Be [46], ^{7}Li [47], and nucleon [48] on ^{208}Pb, with real part in the upper block and imaginary part in the lower one. V_0 and $W_{V,S}$ are the central-nuclear, volume (V) and surface (S) strengths, with $R_{0,V,S}$ and $a_{0,V,S}$ the respective radius and diffuseness parameters, with R_C is the Coulomb radii.

Real part	System	$-V_0$ (MeV)	R_0 (fm)	a_0 (fm)	R_C (fm)		
	^{7}Be + ^{208}Pb	114.2	10.08	0.853	9.41		
	^{7}Li + ^{208}Pb	114.2	7.595	0.853	9.41		
	p + ^{208}Pb	43.03	7.37	0.647	7.27		
	n + ^{208}Pb	29.48	7.37	0.647	–		
Imag. part	**System**	$-W_V$ (MeV)	R_V (fm)	a_V (fm)	$-W_S$ (MeV)	R_S (fm)	a_S (fm)
	^{7}Be + ^{208}Pb	12.40	13.63	0.807	–	–	–
	^{7}Li + ^{208}Pb	9.349	10.27	0.809	–	–	–
	$\binom{\rm p}{\rm n}$ + ^{208}Pb	4.591	7.32	0.647	6.838	7.38	0.627

TABLE III. Numerical limiting parameters, used for the radial integrations (maxima r_{max}, R_{max}, with the respective step sizes Δr and ΔR), for the angular momenta (ℓ_{max}, L_{max}), multipole (λ_{max}), and for bin energy (ε_{max}).

r_{max} (fm)	Δr (fm)	R_{max} (fm)	ΔR (fm)	L_{max} ($\hbar$)	ℓ_{max} ($\hbar$)	λ_{max} ($-$)	ε_{max} (MeV)	
120	0.1	1000	0.05	10000	5	5	10	0.05

^{7}Li-target optical potential parameters did not exhibit any meaningful dependence on the incident energy, hence the same parameters were used for both incident energies. Although we have used different nucleon-target optical potential parameters corresponding to each incident energy, considering the above mentioned global parametrizations, to be short only the ones corresponding to $E_{c.m.}/V_B = 1.5$ are explicit in this table. To minimize the difference in proton and neutron breakups due to their different potentials, the proton-target parameters were also used for neutron-target system, with the required modification in the corresponding depths, V_0. The various integration parameters used in this work are listed in Table III. They were selected based on convergence requirements. The numerical calculations were carried out with the computer code FRESCO [6].

In Fig. 1, to demonstrate that the CDCC method is quite appropriate to describe the systems under investigation, we perform the best fit to elastic scattering cross sections experimental data as functions of the c.m. angle. The data results are obtained from Refs. [33,49], for the ^{8}B + ^{208}Pb and ^{8}Li + ^{208}Pb, respectively. For that, we consider the given potential parameters (ignoring the spin-orbit terms of the proton-target and neutron-target potentials). The effect of breakup processes on both results shown in Fig. 1 could be further investigated by comparing with the cases in which only the projectile ground-states are considered. However, this could be of interest in a different study, as elastic scattering is not the focus of the present work.

III. RESULTS AND DISCUSSION

A. Electric dipole response and Coulomb dissociation

We start with a brief discussion on the structure of the projectiles. For that, the ground-state radial wave functions

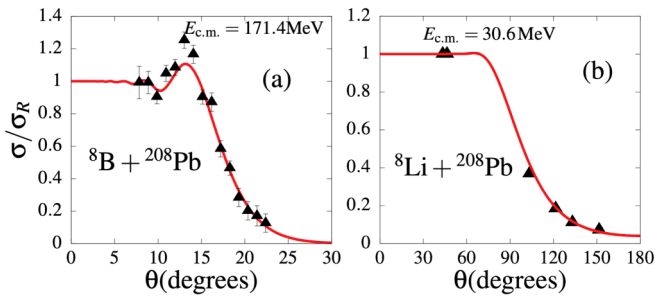

FIG. 1. Elastic scattering cross sections (units of Rutherford σ_R), for the ^{8}B + ^{208}Pb (a) and ^{8}Li + ^{208}Pb (b) reactions, shown as function of the c.m. angle. Experimental data in panels (a) and (b) are, respectively, from Refs. [33,49].

and the integrand of the radial integral in Eq. (16) for all the three systems are presented in Fig. 2. The case where the pure scattering wave function $u^{J_p}_{k\ell}(r)$ is replaced by the bin wave function $\phi^{J_p}_{k_i\ell}(r)$ is also shown. The scattering wave functions were calculated a $E_{c.m.} = 8$ MeV, with $\ell = 2$, $j = 2$. Figures 2(a) and 2(b) show the ground-state wave functions for $\varepsilon_0 = 2.033$ MeV and $\varepsilon_0 = 0.137$ MeV binding energies, respectively. Only for the sake of comparison, the integrands $u^{J_0}_{k_0\ell_0}(r)r^\lambda u^{J_p}_{k\ell}(r)$ and $u^{J_0}_{k_0\ell_0}(r)r^\lambda\varphi_{\alpha_i}(r)$ are shown in Figs. 2(c) and 2(d), respectively. The wave function $\varphi_{\alpha_i}(r)$ is defined in the caption of this figure as a sum of bin wave functions. As expected, it is noticed in this figure that the ^{7}Be +n and ^{7}Li +n bound-state wave functions are similar. They are quite extended in the peripheral region when compared with the ^{7}Be +p wave functions, especially for the lower binding energy. If we were to consider their respective ground-state binding energies, then it is clear from Figs. 2(a) and 2(b) that the ^{7}Be +p wave function has a relatively longer tail compared to that of the ^{7}Li +n system. Considering the two integrands, one observes in Figs. 2(c) and 2(d) that they are much deeper in the interior region ($r \leqslant 10$ fm) for the ^{7}Be +n and ^{7}Li +n neutron-halo systems than for ^{7}Be +p proton-halo system, due to the absence of the Coulomb repulsion in the former cases. In Fig. 2(d), where bin wave functions are used, we notice, unlike in Fig. 2(c), that the superposition of fifty bin wave functions with slightly different bin energies soften the oscillations for distances above 15 fm. This result is suggesting a faster convergence of the radial integral when bin wave functions are considered. We have also verified that the $\int_0^\infty \varphi_{\alpha_i}(r)r^\lambda\varphi_{\alpha_i}(r)dr$ converges rapidly. This approach could be useful to investigate the importance of transitions between continuum states. However, such study is beyond the present proposal.

We also compare the dipole electric response functions, Eq. (16), for the transition the from the p-wave halo ground state to the continuum s and d states, for the three systems. The results, obtained by using RADCAPA code[43], are presented in Fig. 3. They are directly related to the Coulomb dipole breakup cross section by Eq. (17). Again, the same two ground-state binding energies (0.137 and 2.033 MeV) are considered for the three systems.

The electric dipole response function of the ^{7}Be +p system is much below the ones for ^{7}Be +n and ^{7}Li +n, although at higher excitation energies ($\varepsilon = 8$ MeV), the ^{7}Be +p response function slightly overcomes that of ^{7}Li +n, as Fig. 3 shows. Notice that even though the ^{7}Be charge does not play any role on the ^{7}Be +n bound and scattering wave functions, at the first-order transition, the effective charge Z_λ of this system is larger than that of the ^{7}Li +n system. When $\lambda = 1$, from Eq. (15), we obtain $Z_\lambda(^7\text{Be} + n) = -0.5e$, $Z_\lambda(^7\text{Li} + n) = -0.375e$ and $Z_\lambda(^7\text{Be} + p) = 0.375e$. Therefore, the larger value of the ^{7}Be +n response function compared to the ^{7}Li +n one can be mainly understood as due to the effect of the effective charge Z_λ. However, we observe that the ^{7}Be +n electric response function is larger than the ^{7}Be +p one, and this comes from the difference in their effective charges and in the radial integrals, while the ^{7}Li +n electric response function is larger than the one for the ^{7}Be +p system only due to

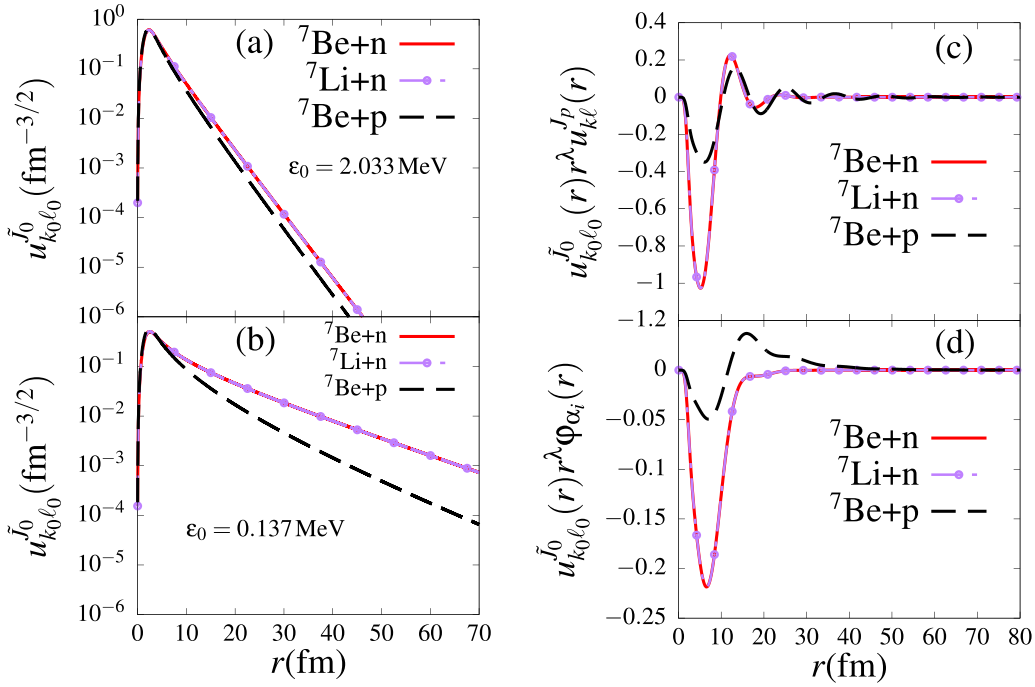

FIG. 2. Ground-state radial p waves, for the "^{8}Be", ^{8}B, and ^{8}Li binding energies 2.033 and 0.137 MeV, as indicated by the legends, are shown in panels (a) and (b). In panel (c), it is shown the radial integrand of the dipole matrix element ($\lambda = 1$) of the ground-state wave function, with the scattering state $j = 2$ and $\ell = 2$, by considering $E_{\rm c.m.} = 8$ MeV for "^{8}Be", ^{8}B, and ^{8}Li. Panel (d) corresponds to panel (c), after replacing the scattering state by the bin wave function $\varphi_{\alpha_i}(r) = \sum_{i=1}^{50} \hat{\phi}_{\alpha_i}(r)$, with the maximum bin energy $\varepsilon_{\rm max} = 8$ MeV. In panels (c) and (d), the bound-state energies are 2.033 MeV for ^{7}Be +n and ^{7}Li +n, being 0.137 MeV for ^{7}Be +p.

the radial integral, given that their effective charges are similar in magnitude.

The Coulomb barrier penetrability in the ^{7}Be +p system damps the continuum wave function at low energies in the region where bound proton wave function is relevant (see Figs. 2(c) and 2(d)) with respect to the ^{7}Li +n one, which explains the strong suppression of the dipole response at low energies seen in Fig. 3. Such effect tends to be less relevant as energy increases and above 7 MeV the ^{7}Be +p dipole response overcomes the ^{7}Li +n one, as the d-wave contribution becomes enhanced by Coulomb scattering. Owing to the larger importance of dipole transition in Coulomb breakup, and given that the reactions at hand are naturally Coulomb-dominated, we expect the Coulomb and total breakup cross sections to follow the trend of the dipole electric response functions. Hence, we anticipate that the conclusions above will remain valid for the breakup cross sections.

As to expose the dependence of the Coulomb breakup cross section on the projectile electric dipole response function, given by Eq. (17), we calculate the ^{8}B + ^{208}Pb first-order Coulomb breakup cross section, by using this equation, comparing the results with experimental data of Ref. [50]. For this purpose, Fig. 4 is presented, with the Coulomb dissociation of ^{8}B on ^{208}Pb at 83 MeV/nucleon, in which the ^{7}Be +p response function is obtained for the transition from the ground to s and d states. As shown, the model results are in excellent agreement with data.

B. Differential elastic breakup cross-sections

To investigate the effects of the charge of the extra proton in ^{7}Be nucleus compared to ^{7}Li, and that of the proton in the ^{7}Be + p system, we first consider the differential breakup cross section. It is well known that in breakup calculations, convergence of the results is a very crucial issue. Therefore, the breakup dynamics of the three ^{7}Be +n, ^{7}Li +n, and ^{7}Be +p systems can be as well compared on the ground of the convergence of their breakup cross sections. To this end, in Fig. 5 we study the convergence of the angular distribution breakup cross sections, with respect to bin energies $\varepsilon_{\rm max}$, for the incident energy above the Coulomb barrier, $E_{\rm c.m.} = 1.50 V_{\rm B}$; although the convergence was also checked in terms of the other numerical integration parameters, such as $\ell_{\rm max}$. The results obtained for $\varepsilon_0 = 2.033$ MeV are displayed in the upper panels [Figs. 5(a), 5(c) and 5(e)], with those for $\varepsilon_0 = 0.137$ MeV in the lower panels [Figs. 5(b), 5(d) and 5(f)]. By inspecting this figure, one notices that an excellent convergence is achieved at $\varepsilon_{\rm max} = 10$ MeV. Therefore, one can argue that, regarding the maximum bin energy required for convergence, there is no meaningful difference between these reactions in the total breakup cross sections angular distributions. A noticeable point, for ε_0=2.033 MeV [Figs. 5(a), 5(c) and 5(e)], is that the convergence rate is faster for ^{7}Be + n and ^{7}Be + p systems, which correspond to the larger core charge. A careful look at these results reveals dislocations of the maxima toward larger angles (with peaks located around

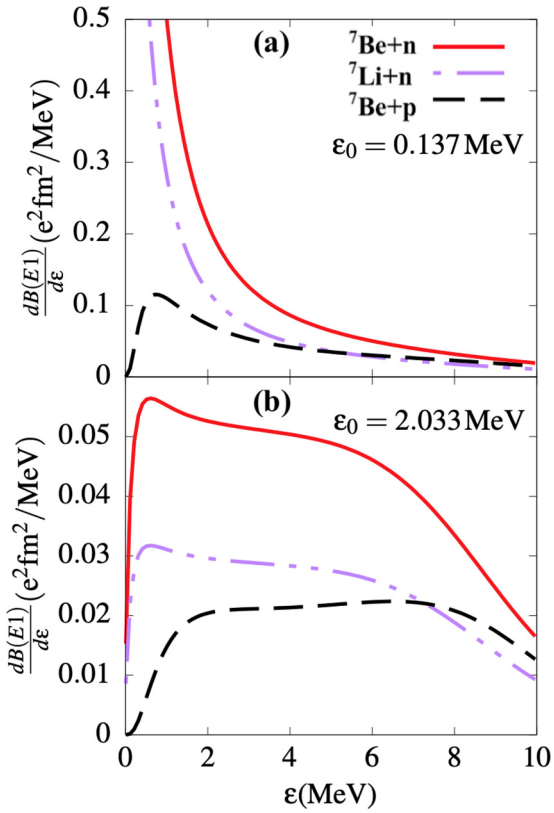

FIG. 3. Electric dipole response functions, as given by Eq. (16), for transition from the p-wave halo ground state to continuum s and d states for ^{7}Be +n, ^{7}Li +n, and ^{7}Be +p systems, for the ground-state energies $\varepsilon_0 = 0.137$ MeV (a) and 2.033 MeV (b).

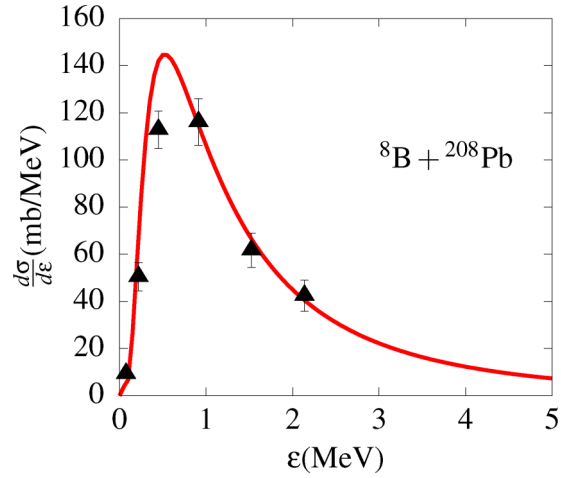

FIG. 4. Cross section for the Coulomb dissociation of ^{8}B on ^{208}Pb at 83 MeV/nucleon (with $v = 0.4065c$ and $\theta_c = 4.3°$, corresponding to $b_{\min} = 12.5$ fm), as given by Eqs. (17) and (18). The behavior, given as a function of the core-nucleon relative energy ε, is compared with data from Ref. [50]. The ^{7}Be +p response function is calculated for the transition from the ground state to s and d states.

30°, 40°, and 50°, for ^{7}Be + n, ^{7}Li + n, and ^{7}Be + p systems, respectively), indicating that the extra ^{7}Be charge tends to confine the breakup cross section to lower angles, whereas the proton charge tends to spread it over a larger angular interval. This tendency also holds for the lower binding energy. The wide spread of the ^{7}Be + p breakup cross section signals a breakup delay caused by the proton tunneling through the core-proton Coulomb barrier, being absent in the other two projectiles, which can be viewed as another main difference between proton- and neutron-halo breakups, apart from the longer neutron-halo ground-state wave function. As this effect is more pronounced for larger binding energies (when the breakup is close to the target, within the nuclear-force range), this spread can be associated with a significant effect of the nuclear breakup. Therefore, in light of the results in Fig. 5 ($\varepsilon_b = 2.033$ MeV), one would expect the ^{7}Be + n breakup to account for the smallest nuclear breakup cross section due to the ^{7}Be charge, and the ^{7}Be + p breakup to the largest nuclear breakup cross section, due to the proton charge. As the binding energy decreases, the breakup process occurs at large distances, where the Coulomb breakup is dominant due to long-range nature of Coulomb forces and short-range nature of nuclear forces. This explains the confinement of all three breakup cross section peaks at small angles ($\theta \leqslant 10°$), enforcing the conclusion that the spread of the breakup cross section in the upper panels is actually a nuclear breakup effect.

For the respective magnitudes of the three breakup cross section peaks, the ^{7}Be+p one is verify to be roughly about one order smaller than the corresponding ones for ^{7}Be +n and ^{7}Li+n systems, which could be anticipated from Figs. 2 and 3. Also, despite the similarities of the ground and continuum wave functions of ^{7}Be +n and ^{7}Li +n (displayed in Fig. 2), the breakup cross section of the latter system is larger than the former one. Therefore, since the static effect due to the ground-state wave function is about the same in both the cases, the difference should come from a three-body dynamical effect, expressed by the virtual excitation of the nucleon-core continuum states, associated with a large electric response function for the ^{7}Be + n system compared to that of the ^{7}Li + n system (as shown in Fig. 3). It follows that the relevant differences on the breakup cross sections of ^{7}Be + n and ^{7}Be + p cannot be attributed only to the large extension of the ground-state wave function of the ^{7}Be + n. These results are clearly emphasizing the dynamical effect of the core nucleus charge on the breakup process.

The different core-nucleon continuum partial-wave contributions to the differential breakup cross sections, with respect to the relative energy distributions of the fragments, are shown in Fig. 6, up to d waves, to further assess the importance of the core charge and proton charge in the three-body breakup dynamics, as well as to verify how the transition to continuum states are affected. As in Fig. 5, both binding energies are considered for the same incident energy above the Coulomb barrier. The nucleon-core final state interaction (FSI) reveals being a dominant mechanism to build the excitation energy spectrum. The order in which the partial-waves contribute to the total cross section appear to remain unchanged for all three systems. The s and $p_{3/2}$ wave contributions are largely dominant at lower excitation energies and become substantial for the lower binding energy. In Fig. 6(e), the $p_{3/2}$-wave contribution overcomes the s-wave contribution at $\varepsilon \geqslant 1$ MeV.

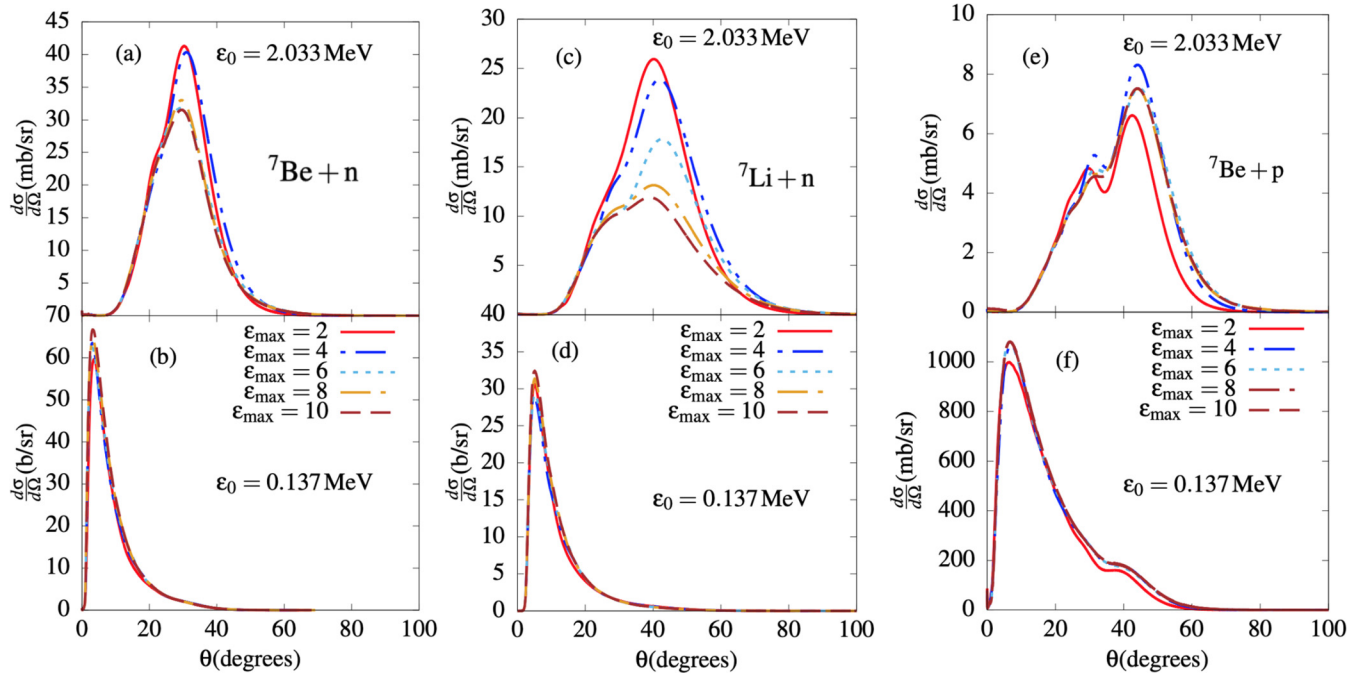

FIG. 5. The angular distributions of the total differential breakup cross sections, obtained from Eq. (13), are shown in terms of the c.m. angle of the core with the incident direction, are given at $E_{\text{c.m.}}/V_{\text{B}} = 1.50$, in terms of the maximum bin energies ε_{max} (indicated inside the lower frames), for $\varepsilon_0 = 2.033$ MeV (upper frames) and 0.137 MeV (lower frames). Note that in panels (b) and (d), $d\sigma/d\Omega$ is given in units of b/sr, whereas in the other cases it is given in mb/sr.

Although there is a qualitative similarity between the results in Figs. 6(a)–6(f), they reveal the final state interaction due to the proton-core Coulomb, where the maximum of each partial wave is pushed to larger values of the relative energy, which suggest that in the ^{8}B projectile the proton in the halo due to the Coulomb interaction gains relative momentum. The large

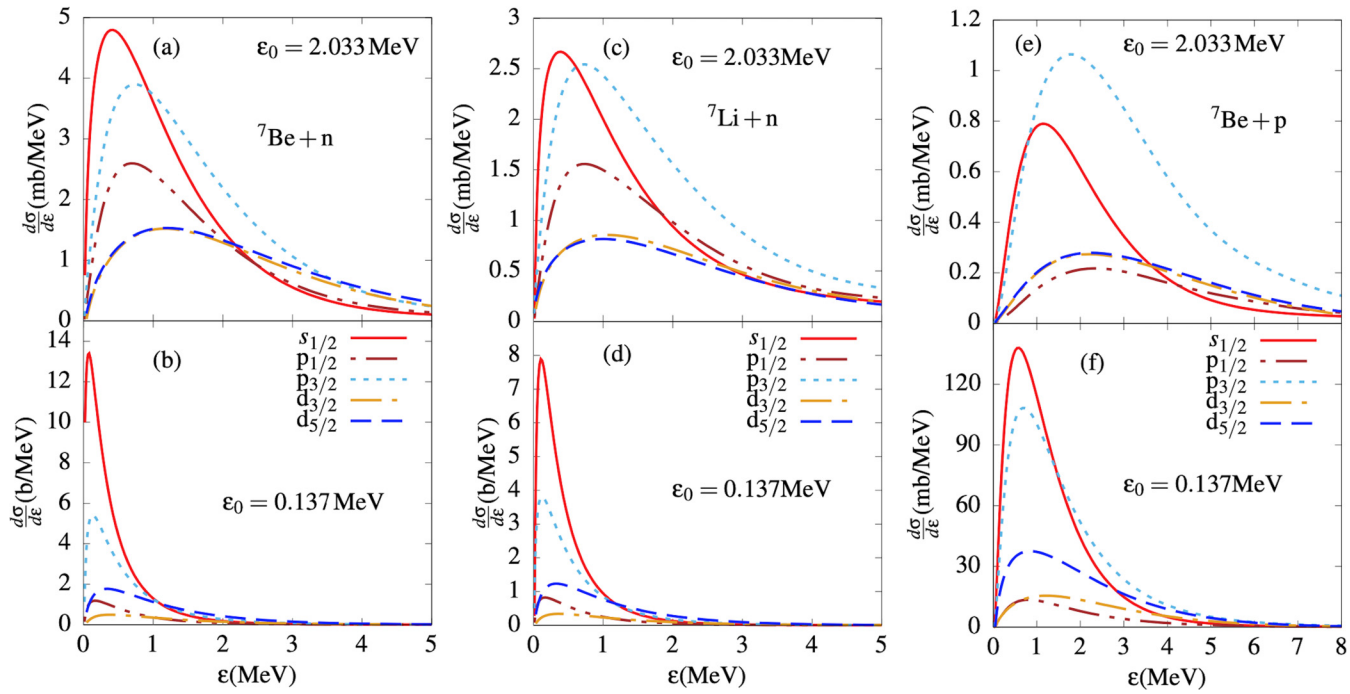

FIG. 6. Total relative angular momentum partial wave contributions to the total breakup differential cross section $d\sigma/d\varepsilon$, given as functions of the core-nucleon relative energy distributions ε, obtained at $E_{\text{c.m.}}/V_{\text{B}} = 1.50$, for the binding energies $\varepsilon_0 = 2.033$ MeV (upper frames) and 0.137 MeV (lower frames). The partial waves are being identified inside the lower frames. Note that in panels (b) and (d), $d\sigma/d\varepsilon$ is given in units of b/MeV, whereas in the other cases it is given in mb/MeV.

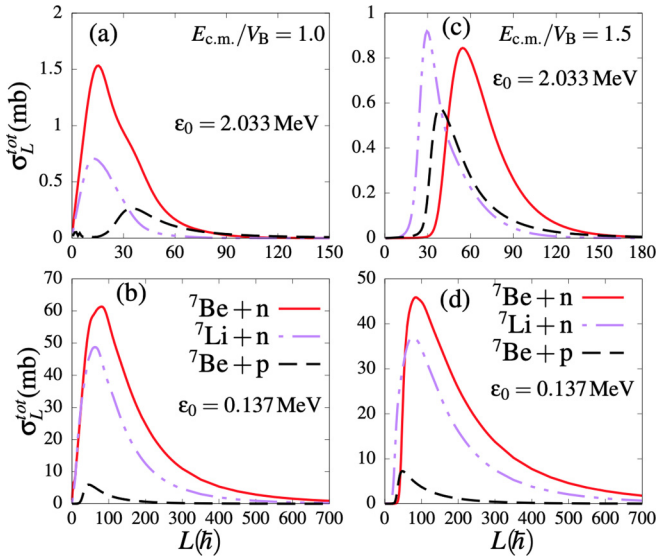

FIG. 7. Projectile-^{208}Pb relative angular distribution of the total breakup cross sections, for ^{7}Be +n, ^{7}Li +n, and ^{7}Be +p projectiles at $E_{c.m.}/V_B = 1.0$ [panels (a) and (b)] and 1.5 [panels (c) and (d)], for $\varepsilon_0 = 2.033$ MeV [panels (a) and (c)], and 0.137 MeV [panels (b) and (d)].

enhancement of the partial waves in particular the s and $p_{3/2}$ in the neutron-halo case when the neutron-core potential is tuned to provide a weakly bound p-wave bound state also enhances the s-wave scattering length, showing such large grow in partial wave the cross-section shown in Figs. 6(b) and 6(d). In the proton-halo case, the relative Coulomb barrier between the fragments, pushes the peaks to higher relative energies, while damping the magnitude of the cross-section relative to the neutron-halo cases, owing the the penetration factor in the Coulomb barrier brought in by the FSI between the two charged fragments.

C. Angular momentum distribution of elastic breakup cross-sections

The relevance of the core-target interaction to the three-body reaction dynamics can be accessed by the projectile-target orbital angular momentum distributions of the total, Coulomb and nuclear breakup cross sections, through the results shown in Figs. 7 and 8, which can better display the breakup cross section behavior in the interior (nuclear dominated) and peripheral (Coulomb dominated) regions. However, separating the total breakup cross section into its Coulomb and nuclear components is not trivial, due to the importance of Coulomb-nuclear interference, as discussed in Ref. [27]. In the present work, we adopt an approximate procedure, where the Coulomb breakup cross-section is obtained by switching off the nuclear interaction of the fragments with the target in the coupling matrix elements, only returning its diagonal part to account for the nuclear absorption in the diagonal channel. Likewise, the nuclear breakup cross section is obtained by switching off the off-diagonal Coulomb interaction. This approach, although approximate, has been widely adopted, since introduced in early works [10,51], to obtain the

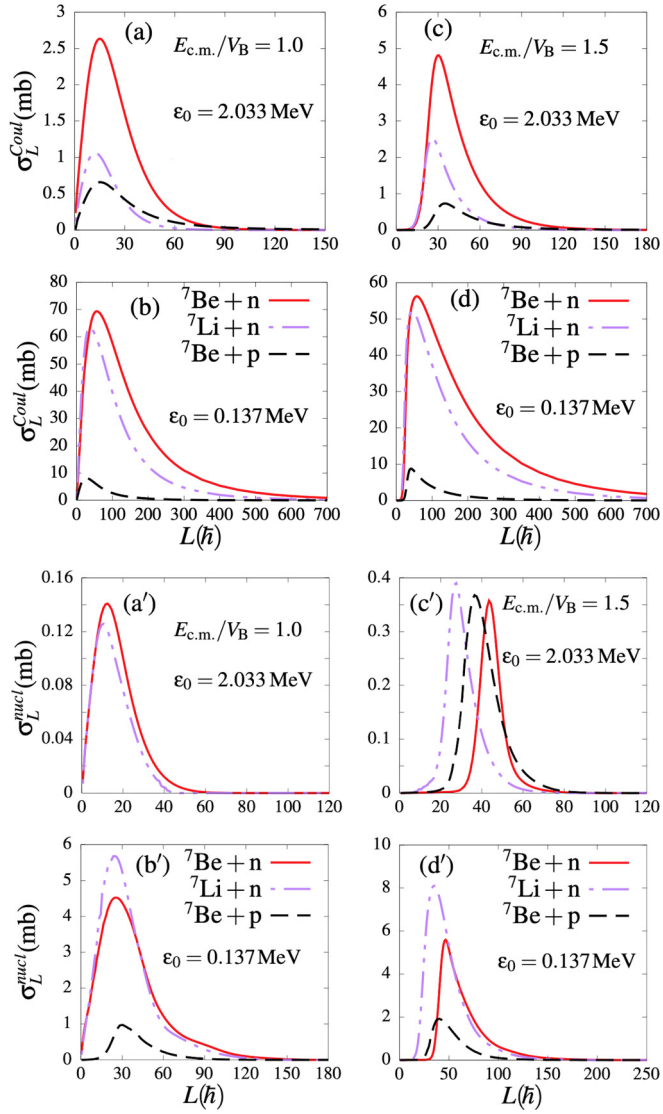

FIG. 8. In correspondence with the four panels shown in Fig. 7, this figure presents the corresponding Coulomb [upper (a)–(d) frames] and Nuclear [lower (a′)–(d′) frames] breakup cross sections.

Coulomb and nuclear breakup cross sections. The approach proposed in Ref. [27] can be a better alternative, although its numerical implementation is not so straightforward. We then refer to "total" breakup cross section, the one that is obtained with both Coulomb and nuclear interactions simultaneously included in the coupling matrix elements.

For the three core-nucleon projectiles we are considering, in Fig. 7 we present the corresponding angular momentum distributions of the total breakup cross sections $\sigma_L^{\rm tot}$. The results are shown for two incident energies (relative to the Coulomb barrier), with both two binding energies under consideration (2.033 and 0.137 MeV). In Figs. 7(a) and 7(b), for incident energy at the barrier, where the Coulomb repulsion is stronger, we notice that σ_L of both ^{7}Be + n and ^{7}Li + n systems are similar at very lower angular momenta, whereas that of ^{7}Be + p is much lower. In the peripheral region (larger

angular momenta), where Coulomb breakup is dominant, we notice that the ^{7}Be +n breakup cross section is more extended than the ^{7}Li +n one. When considering the two lower panels, Figs. 7(b) and 7(d), for $\varepsilon_0 = 0.137$ MeV, a fair similarity between the results are verified, even though the two panels correspond to different incident energies. The fact is that for lower binding energy, the breakup becomes more peripheral, favoring the Coulomb breakup at the expense of the nuclear breakup. Because both ^{7}Be +n and ^{7}Li +n systems have similar static effects (same ground-state wave function), among other factors, the difference in their breakup cross-sections (in the peripheral region) comes from the contribution of the Coulomb potentials from the charge of the extra proton, in ^{7}Be nucleus, which is expected to increase the Coulomb breakup cross section.

The distinctive manifestation of the three-body dynamics in the inner interaction region, namely, where the nuclear potentials are active, is illustrated in Fig. 7(c), for $E_{\rm c.m.}/V_B = 1.5$. Here two factors are responsible for the contribution of the nuclear breakup be enhanced in comparison to the other panel results: slightly weak Coulomb repulsion and large breakup probability due to the vicinity of the target (i.e., within the range of nuclear forces). This panel shows that the $\sigma_L^{\rm tot}$ of ^{7}Be +n system is pushed more towards larger L, being suppressed for $L \leqslant 30\hbar$. In a similar behavior, $\sigma_L^{\rm tot}$ for the ^{7}Be +p system is suppressed for $L \leqslant 20\hbar$. To understand this, we recall that we have a Coulomb-dominated reaction at hand, regardless the ground-state binding energy (as will be shown), and the Coulomb breakup is dominated by dipole transition. In an event where the projectile effective charge interacts with the target charge, one obtains for ^{7}Be +n, ^{7}Li +n, and ^{7}Be +p systems that $|Z_\lambda Z_T| = +41e^2, +30.75e^2$, and $+30.75e^2$. Therefore, in this case, ^{7}Be +n system accounts for the strongest Coulomb repulsion, hence weakest nuclear contribution. This agrees with our assessment in Sec. III B, that the extra ^{7}Be proton is to confine the breakup cross section at lower angles. The difference observed in the breakup cross sections for ^{7}Li +n and ^{7}Be +p systems can be, among other factors, ascribed to their different static effect.

To display the relative relevance of the nuclear (inner region) and Coulomb (peripheral region) breakup cross section angular distribution, shown in Fig. 7, we separate in two blocks of Fig. 8 the corresponding contributions of the projectile-target orbital angular momentum distributions. The Coulomb/nuclear L distributions of the breakup cross-section are obtained by the upper/lower four blocks, when the nuclear/Coulomb interactions of the fragments with the target is switched off in the coupling matrix elements, as we have previously explained. One observes in this figure the particular similarity of Figs. 8(a), 8(b) and 8(d) (for $\sigma_L^{\rm Coul}$) with the corresponding Figs. 7(a), 7(b) and 7(d), whereas the $\sigma_L^{\rm nucl}$ shown in Fig. 8(c) is similar to the interior region part of Fig. 7(c).

It is a known fact that, for loosely bound systems, nuclear forces stretch beyond the $R_n = r_0(A_p^{1/3} + A_t^{1/3})$ fm. To check this and better understand the peaks of the different nuclear cross sections, at specific values of L shown in Figs. 8(a′)–8(d′), we first determine the corresponding grazing angular momentum,

$$L_{\rm gr} = \sqrt{(2\mu_{\rm pt}/\hbar^2)(E_{\rm c.m.} - \varepsilon_0)}\, R_n, \tag{19}$$

which are summarized in Table IV, for $r_0 = 1.2$ fm.

TABLE IV. Grazing angular momenta $L_{\rm gr}$, as defined in Eq. (19), with $V_B = 38.91$, 28.65, and 49.36 MeV for the reactions with projectiles ^{8}Be, ^{8}Be, and ^{8}Be, respectively, for the given ε_0 binding energies.

Systems	^{7}Be + n		^{7}Li + n		^{7}Be +p	
ε_0(MeV)	2.033	0.137	2.033	0.137	2.033	0.137
$E_{\rm c.m.} = V_{\rm B}$	35	36	30	31	40	41
$E_{\rm c.m.} = 1.5V_{\rm B}$	43	44	37	38	49	50

Considering these values and by looking closely to the corresponding panels of Fig. 8, one first notices that the nuclear breakup cross sections are largely extended beyond the grazing angular momenta. For example, in Fig. 8(a′), the ^{7}Li +n and ^{7}Be +n cross sections are stretched up to $L = 40\hbar$ and $L = 60\hbar$, respectively, while the respective grazing angular momenta are $L_{\rm gr} = 30\hbar$ and $L_{\rm gr} = 35\hbar$. The longer tails of nuclear breakup cross sections beyond the grazing angular momenta, prove that nuclear forces are stretched beyond R_n in all three cases. Such property is due to the extended tail of the bound-state wave function of the weakly bound halo nucleon in the projectile. Looking again closely at the corresponding panels of Fig. 8, one observes that for the neutron-halo systems, the different cross section peaks are located around the grazing angular momenta.

D. Integrated Total, Coulomb, and Nuclear elastic breakup cross-sections

To get more insight into the conclusions that we are so far drawing, providing additional relevant elements for a qualitative analysis, we consider the integrated total, Coulomb, and nuclear breakup cross sections, which are presented in Table V. As anticipated by the analysis of results presented in Fig. 5, for $E_{\rm c.m.}/V_{\rm B} = 1.5$, the nuclear breakup is relatively more important in the ^{7}Be + p system (particularly for larger binding energies), in comparison to the other two systems, as can be checked in the table. This is attributed to the breakup delay caused by the proton tunneling through the proton-^{7}Be Coulomb barrier, which is a distinctive effect not present in ^{7}Li + n and ^{7}Be + n systems.

Table V also shows a substantial enhancement of the ^{7}Be + n and ^{7}Li + n total and Coulomb breakup cross sections over their ^{7}Be + p counterparts. When the binding energy increases ($\varepsilon_0 = 2.033$ MeV), the neutron-rich total and Coulomb breakup cross sections are substantially reduced compared to their proton-rich counterparts. For instance, by considering the incident energy at the barrier, the ^{7}Be +p total cross section is reduced by a factor of about 46, while the ones for ^{7}Be +n and ^{7}Li +n are, respectively, reduced by a factors of about 238 and 394.

We recall that the only difference between the ^{7}Be + n and ^{7}Li + n projectile systems is the extra proton charge in the ^{7}Be

TABLE V. Coulomb and nuclear integrated breakup cross sections (in mb units) for the ^{7}Be +p, ^{7}Be +n and ^{7}Li +n reactions on a lead target at incident energies $E_{\rm c.m.} = V_{\rm B}$ and 1.50 $V_{\rm B}$, for $\varepsilon_0 =$ 0.137 MeV and $\varepsilon_0 = 2.033$ MeV binding energies. The last line, for each incident energy, $\delta_{\rm x}^{\rm BeLi} \equiv \sigma_{\rm x}^{^7{\rm Be+n}} - \sigma_{\rm x}^{^7{\rm Li+n}}$ (x ≡ tot, C, nucl) is furnishing the quantitative effect in the cross sections, provided by a one-unit-charge difference in the projectile core nuclei.

		$\varepsilon_0 = 0.137$ MeV			$\varepsilon_0 = 2.033$ MeV		
$E_{\rm c.m.}$	Systems	$\sigma_{\rm tot}$	σ_C	$\sigma_{\rm nucl}$	$\sigma_{\rm tot}$	σ_C	$\sigma_{\rm nucl}$
	^{7}Be +p	524.8	735.5	29.3	11.38	25.40	1.70
$V_{\rm B}$	^{7}Be +n	11990	13070	205.0	50.42	84.57	3.07
	^{7}Li +n	7393	8777	218.2	18.75	26.66	2.48
	$\delta_{\rm x}^{\rm BeLi}$	**4597**	**4293**	**−13.2**	**31.67**	**57.91**	**0.59**
	^{7}Be +p	732.1	820.8	65.52	21.64	26.07	7.07
$1.5V_{\rm B}$	^{7}Be +n	10630	12390	186.6	34.94	154.50	4.50
	^{7}Li +n	7274	8613	303.0	25.34	64.74	6.12
	$\delta_{\rm x}^{\rm BeLi}$	**3356**	**3777**	**−116.4**	**9.6**	**89.76**	**−1.62**

core nucleus. To estimate the quantitative effect of this extra charge on the different breakup cross sections, we define the difference $\delta_{\rm x}^{\rm BeLi} = \sigma_{\rm x}^{^7{\rm Be+n}} - \sigma_{\rm x}^{^7{\rm Li+n}}$ (x ≡ tot, C, nucl), where $\sigma_{\rm x}^{^7{\rm Be+n}}$ and $\sigma_{\rm x}^{^7{\rm Li+n}}$ are the integrated breakup cross sections corresponding to $^7{\rm Be} + n$ and $^7{\rm Li} + n$ systems, respectively. Notice that the nonzero $\delta_{\rm x}^{\rm BeLi}$ can only be attributed to the extra proton charge in ^{7}Be with respect to ^{7}Li. While these core nuclei charges differ by just one unit, the verified difference in their breakup cross sections is quite remarkable for $\varepsilon_0 = 0.137$ MeV. Essentially, this table is clarifying that the dynamical effect of the extra proton's charge in the ^{7}Be core nucleus will enhance substantially the total and Coulomb breakup cross sections, while it lowers the nuclear breakup cross section. As we have already argued, this effect is manifested through the dipole electric response function, as shown in Fig. 3.

The effect of the extra charge in the projectile core nucleus can further be estimated by also considering the ratio $\delta_{\rm x}^R(\%) = \delta_{\rm x}^{\rm BeLi}/\sigma_{\rm x}^{^7{\rm Be+n}}$, which is presented in the following Table VI.

It is shown that the dynamical effect of this extra charge, accounts for more than 30% of the $^7{\rm Li} + n$ total and Coulomb breakup cross sections for $\varepsilon_0 = 0.137$ MeV, and much more for $\varepsilon_b = 2.033$ MeV. These results serve to further expose the importance of the charge of the core nucleus in the breakup process.

TABLE VI. Ratios $\delta_{\rm x}^R = \delta_{\rm x}^{\rm BeLi}/\sigma_{\rm x}^{^7{\rm Be+n}}$ obtained from the differences $\delta_{\rm x}^{\rm BeLi}$ and the corresponding integrated breakup cross sections $\sigma_{\rm x}^{^7{\rm Be+n}}$ defined in Table V.

$E_{\rm c.m.}/V_{\rm B}$	$\varepsilon_0 = 0.137$ MeV			$\varepsilon_0 = 2.033$ MeV		
	$\delta_{\rm tot}^R$	$\delta_{\rm C}^R$	$\delta_{\rm nucl}^R$	$\delta_{\rm tot}^R$	$\delta_{\rm C}^R$	$\delta_{\rm nucl}^R$
1.0	38%	33%	−6%	63%	68%	19%
1.5	32%	30%	−62%	27%	58%	−36%

IV. CONCLUSIONS

We have presented a detailed comparative analysis of the breakup cross section of three equal-mass projectiles ^{8}B, ^{8}Li, and "^{8}Be" on a lead target, by considering each projectiles under two possible weakly bound ($\varepsilon_0 = 0.137$ MeV and 2.033 MeV) configurations, as ^{7}Be +p, ^{7}Li +n, and ^{7}Be +n, for incident energies at the Coulomb barrier and above. The projectile binding energies $\varepsilon_0 = 0.137$ MeV and 2.033 MeV, correspond to the well-known ^{7}Be +p and ^{7}Li +n systems, whereas the fictitious ^{7}Be +n bound state was assumed with these energies to provide support to our comparative analysis. Our main goal was to investigate whether some previous conclusions drawn in the study of one-nucleon (neutron or proton) weakly bound projectiles on a heavy target are exclusively static effects due to the ground-state binding energy and the charge of the valence nucleon [20,29]. Thus, we investigated both the manifestation of the static and three-body dynamical effects in these reactions. To expose the consequences of the three-body dynamics, we compared the ^{7}Be +n and ^{7}Li +n breakup cross sections. To minimize the effect of the ground-state binding energy in our calculations, in the three examples we have assumed the same fixed values ε_0 corresponding to the experimental ^{7}Be +p and ^{7}Li +n binding energies, such that two different calculations were performed for each reaction. Starting with the internal structures of these systems, we obtained that although the ground and continuum wave functions of the ^{7}Be +n and ^{7}Li +n systems are similar, their dipole electric response functions are quite different, with that of the ^{7}Be +n system being enhanced due to the dipole effective charge, which is larger in the latter system than in former. Consequently, as the reactions are Coulomb-dominated, with the Coulomb breakup cross section directly proportional to the dipole electric response function, larger total and Coulomb breakup cross sections are obtained for ^{7}Be +n than for ^{7}Li +n. Therefore, this point out that the contribution of the charge of the extra proton in the ^{7}Be +n core nucleus is relevant for the three-body reaction dynamics. In fact, it is deduced that the contribution of the extra charge to the three-body reaction dynamics represents about 30% of the total and Coulomb breakup cross sections. However, this effect is negative on the nuclear breakup cross section: it accounts for −62% for the incident energy above the Coulomb barrier, when $\varepsilon_0 = 0.137$ MeV; and about −36%, when $\varepsilon_0 =$ 2.033 MeV. These results showed that both static and three-body dynamical effects are behind the relevance of the ^{7}Be +n breakup cross sections over the corresponding breakups for ^{7}Be +p. For the incident energy above the Coulomb barrier, it is obtained that the proton tunneling through the proton-core Coulomb barrier, delays the ^{7}Be +p breakup process, resulting in a wide spread of the corresponding breakup cross section over a large angular interval, which increases the nuclear breakup contribution. The core charge in the ^{7}Be +n system confines the breakup cross section at lower angles (large distances), which results in the increase of the Coulomb breakup cross section. However, the results indicated that when a proton is replaced by a neutron in the study of proton- and neutron-halo breakups, not only this has an effect on the ground-state wave function, but also affects the interaction of

the same core nucleus with the target. Therefore, our conclusion is that a large tail of the neutron-halo ground-state wave function is not the only reason why, when considered identical ground-state binding energies, neutron-halo breakup cross sections are larger than proton-halo breakup cross sections, as it is widely understood.

The angular dependence of the breakup cross section exhibits the strong interplay between static and three-body dynamical effects, changing the relative importance of the nuclear breakup against the Coulomb one, as already mention in Ref. [52]. The Coulomb interaction between the proton and the core shows its effects in an enhancement of the forward cross section for the small proton separation energy ($\varepsilon_0 = 0.137$ MeV) in ^{8}B. By increasing this energy to $\varepsilon_0 = 2.033$ MeV (as in ^{7}Li +n) the nuclear breakup becomes more relevant, but its importance depends on the target absorption. The peak of the spectrum distribution is moved to higher relative energies, while damping its magnitude with respect to the neutron-halo case, owing to the Coulomb barrier penetration factor brought in by the FSI between charged fragments. This feature of the two-body dynamics immersed in the three-body system in the proton-halo breakup, evidences once more the interplay between static and dynamical effects, being unique for the proton-halo system and not present in the neutron-halo breakup.

The results and analysis presented here provide further understanding on the proton-and neutron-halo breakups when considering heavy target. As for light targets, where the nuclear breakup is dominant, or medium ones, when the contribution from the nuclear breakup is not negligible compared to the Coulomb breakup, it would be important to perform similar analysis. In this case, one would expect that the manifestation of the three-body dynamics from the contribution associated with the charge of the extra proton in the ^{7}Be core nucleus to be much less important. Within the same perspective, one could also study the dependence of the breakup process on the mass of the core nucleus. In this regard, the analysis of ^{7}Be +n, ^{8}Be +n, and ^{10}Be +n breakups on heavy targets would be interesting, as all three systems have the same charge, but different effective charges.

ACKNOWLEDGMENTS

We acknowledge support from Conselho Nacional de Desenvolvimento Científico e Tecnológico [Projects No. 308486/2015-3 (T.F.), No. 304469-2019-0 (L.T.), and INCT-FNA Project No. 464898/2014-5], Fundação de Amparo à Pesquisa do Estado de São Paulo [Project No. 2017/05660-0 (L.T. and T.F.)].

[1] R. Chatterjee and R. Shyam, Prog. Part. Nucl. Phys. **103**, 67 (2018).
[2] A. Bonaccorso, Prog. Part. Nucl. Phys. **101**, 1 (2018).
[3] L. F. Canto, P. R. S. Gomes, R. Donangelo, J. Lubian, and M. S. Hussein, Phys. Rep. **596**, 1 (2015).
[4] J. Gómez-Camacho and A. M. Moro, A pedestrian approach to the theory of transfer reactions: application to weakly bound and unbound exotic nuclei, in *The Euroschool on Exotic Beams*, 4th ed., Lecture Notes in Physics, Vol. 879, edited by C. Scheidenberger and M. Pfutzner (Springer, Heidelberg, 2014).
[5] N. Keeley, N. Alamanos, K. W. Kemper, and K. Ruseka, Prog. Part. Nucl. Phys. **63**, 396 (2009).
[6] I. J. Thompson and F. M. Nunes, *Nuclear Reactions for Astrophysics* (Cambridge University Press, New York, 2009).
[7] N. Keeley, R. Raabe, N. Alamanos, and J. L. Sida, Prog. Part. Nucl. Phys. **59**, 579 (2007).
[8] L. F. Canto, P. R. S. Gomes, R. Donangelo, and M. S. Hussein, Phys. Rep. **424**, 1 (2006).
[9] Y. Suzuki, K. Yabana, R. G. Lovas, and K. Varga, *Structure and Reactions of Light Exotic Nuclei* (Taylor & Francis Group, London/New York, 2003).
[10] F. M. Nunes and I. J. Thompson, Phys. Rev. C **57**, R2818 (1998).
[11] V. Guimarães *et al.*, Phys. Rev. Lett. **84**, 1862 (2000).
[12] L. Trache *et al.*, Phys. Rev. C **67**, 062801(R) (2003).
[13] A. M. Moro, R. Crespo, H. García-Martínez, E. F. Aguilera, E. Martínez-Quiroz, J. Gómez-Camacho, and F. M. Nunes, Phys. Rev. C **68**, 034614 (2003).
[14] P. Capel and D. Baye, Phys. Rev. C **71**, 044609 (2005).
[15] G. Goldstein, D. Baye, and P. Capel, Phys. Rev. C **73**, 024602 (2006).
[16] K. Ogata, S. Hashimoto, Y. Iseri, M. Kamimura, and M. Yahiro, Phys. Rev. C **73**, 024605 (2006).
[17] G. Goldstein, P. Capel, and D. Baye, Phys. Rev. C **76**, 024608 (2007).
[18] J. Lubian, T. Correa, E. F. Aguilera, L. F. Canto, A. Gomez-Camacho, E. M. Quiroz, and P. R. S. Gomes, Phys. Rev. C **79**, 064605 (2009).
[19] E. F. Aguilera *et al.*, Phys. Rev. C **79**, 021601(R) (2009).
[20] R. Kumar and A. Bonaccorso, Phys. Rev. C **84**, 014613 (2011).
[21] Y. Kucuk and A. M. Moro, Phys. Rev. C **86**, 034601 (2012).
[22] B. Paes, J. Lubian, P. R. S. Gomes, and V. Guimarães, Nucl. Phys. A **890**, 1 (2012).
[23] B. Mukeru and M. L. Lekala, Phys. Rev. C **91**, 064609 (2015).
[24] B. Mukeru, M. L. Lekala, and A. S. Denikin, Nucl. Phys. A **935**, 18 (2015).
[25] B. Mukeru, M. L. Lekala, and G. J. Rampho, J. Phys. G: Nucl. Part. Phys **42**, 085110 (2015).
[26] B. Mukeru, M. L. Lekala, and A. S. Denikin, J. Phys. G: Nucl. Part. Phys. **42**, 015109 (2015).
[27] P. Descouvemont, L. F. Canto, and M. S. Hussein, Phys. Rev. C **95**, 014604 (2017).
[28] P. Descouvemont and E. C. Pinilla, Few-Body Syst. **60**, 11 (2019).
[29] J. Rangel, J. Lubian, L. F. Canto, and P. R. S. Gomes, Phys. Rev. C **93**, 054610 (2016).
[30] M. S. Gautam, Chin. Phys. C **40**, 054101 (2016).
[31] P. Capel and Y. Nollet, Phys. Rev. C **96**, 015801 (2017).
[32] G. A. Korolev *et al.*, Phys. Lett. B **780**, 200 (2018).
[33] Y. Y. Yang, X. Liu, D. Y. Pang, D. Patel, R. F. Chen, J. S. Wang *et al.*, Phys. Rev. C **98**, 044608 (2018).
[34] B. Mukeru, J. Phys. G: Nucl. Part. Phys. **45**, 065201 (2018).

[35] G. Baur, K. Hencken, and D. Trautmann, Prog. Part. Nucl. Phys. **51**, 487 (2003).
[36] C. A. Bertulani and G. Baur, Phys. Rep. **163**, 299 (1988).
[37] G. Baur and H. Rebel, Annu. Rev. Nucl. Part. Sci. **46**, 321 (1996).
[38] K. Alder, A. Bohr, T. Huus, B. Mottelson, and A. Winther, Rev. Mod. Phys. **28**, 432 (1956).
[39] L. C. Chamon, B. V. Carlson, L. R. Gasques, D. Pereira, C. De Conti, M. A. G. Alvarez, M. S. Hussein, M. A. Cândido Ribeiro, E. S. Rossi Jr., and C. P. Silva, Phys. Rev. C **66**, 014610 (2002).
[40] N. Austern, Y. Iseri, M. Kamimura, M. Kawai, G. Rawitscher, and M. Yahiro, Phys. Rep. **154**, 125 (1987).
[41] M. Abramowitz and I. Stegun, *Handbook of Mathematical Functions: with Formulas, Graphs, and Mathematical Tables* (National Bureau of Standards, Washington, D.C., 1964).
[42] Y. Iseri, M. Yahiro, and M. Kamimura, Prog. Theor. Phys. Suppl. **89**, 84 (1986).
[43] C. A. Bertulani, Comput. Phys. Commun. **156**, 123 (2003).
[44] M. Wang *et al.*, Chin. Phys. C **41**, 030003 (2017); see also https://www.nndc.bnl.gov/nudat2/.
[45] H. Esbensen and G. F. Bertsch, Nucl. Phys. A **600**, 37 (1996).
[46] S. J. Wang *et al.*, J. Phys. Conf. Ser. **420**, 012075 (2013).
[47] J. Cook, Nucl. Phys. A **388**, 153 (1982).
[48] A. J. Koning and J. P. Belaroche, Nucl. Phys. A **713**, 231 (2003).
[49] J. J. Kolata, V. Z. Goldberg, L. O. Lamm, M. G. Marino, C. J. OKeeffe, G. Rogachev *et al.*, Phys. Rev. C **65**, 054616 (2002).
[50] B. Davids, D. W. Anthony, T. Aumann, S. M. Austin, T. Baumann, D. Bazin *et al.*, Phys. Rev. Lett. **86**, 2750 (2001).
[51] F. M. Nunes and I. J. Thompson, Phys. Rev. C **59**, 2652 (1999).
[52] A. Di Pietro, A. M. Moro, J. Leib, and R. de Diego, Phys. Lett. B **798**, 134954 (2019).